RSC Advances

ROYAL SOCIETY OF CHEMISTRY

PAPER

View Article Online
View Journal | View Issue

Check for updates

Cite this: *RSC Adv.*, 2023, **13**, 2993

Bi_2O_3 modified TiO_2 nanotube arrays and their application towards unsymmetrical dimethylhydrazine degradation in wastewater by electroassisted photocatalysis†

YiZhi Zeng,[a] Feng Zhou*[a] and Yuan Gao[b]

Received 21st September 2022
Accepted 17th December 2022

DOI: 10.1039/d2ra05953c

rsc.li/rsc-advances

In the present research, the preparation process parameters of TiO_2 nanotube arrays (TNAs) prepared by anodic oxidation were systematically studied by the orthogonal experimental method for the first time. Herein, the parameters of nine factors were optimized; the optimal parameters were: the electrolyte was a 0.2 mol L^{-1} NaF solution with 3% vol H_2O at pH 7, the anodic oxidation voltage was 40 V, the electrode spacing was 4 cm and the reaction was carried out for 60 minutes. The physicochemical properties of the materials were characterized by SEM, XRD, EDS, UV-vis, and PL spectroscopy. By electrodeposition of Bi_2O_3 modified TNAs, the degradation rate of unsymmetrical dimethylhydrazine (UDMH) wastewater on the TNAs-10 was 89.14% within 10 h, which was 2.69 times that on pure TNAs. A bias potential of +0.3 V (*vs.* open circuit potential) was applied to the modified TNAs-10. The degradation rate of UDMH was significantly enhanced on the TNAs-10 (bias) process as compared to the TNAs-10 process. The degradation rate of UDMH wastewater on TNAs-10 (bias) exhibited an exponential distribution. UDMH and its toxic by-products FDMH, NDMA were completely degraded after 8 h.

1 Introduction

Environmental pollution and energy shortage have seriously affected human survival and social development. UDMH is widely used as a propellant in aerospace and military fields,[1] and a large amount of UDMH wastewater is produced. UDMH and its by-products, such as *N*-nitrosodimethylamine (NDMA) and formaldehyde dimethyl hydrazone (FDMH), are considered carcinogenic toxins and represent a serious health hazard to the population.[2,3] Therefore, the demand for the treatment of UDMH wastewater is requisite. There are many conventional treatment methods for the UDMH wastewater, which can be classified as physical, chemical, and biological methods. Traditional physical techniques such as adsorption by activated carbon, ion exchange and incineration were not appropriate for the treatment of UDMH wastewater due to the regeneration of adsorbents and resins as well as contamination by products of incomplete incineration. Chemical methods, such as $H_2O_2/O_3/$UV, catalytic oxidation of Cu, Fe, and Co salts combined with H_2O_2/O_3 (*i.e.*, heterogeneous Fenton) are trapped in the need to continue to produce O_3, resulting in high energy consumption and high operating costs.[4] Liang, *et al.*[5] degraded UDMH by the method of catalytic wet peroxide oxidation (CWPO) with CuO/ZnO/NiO/g-Al_2O_3, Cu^{2+} and H_2O_2. However, it would cause secondary pollution due to the difficulty in recycling metal ions. In addition, hydrogen peroxide was consumed and excess H_2O_2 need to be removed with MnO_2. Biological methods have been developed to treat UDMH-containing wastewater, including plant and microbiological methods. It requires longer reaction time, as a result, could not meet the demand for treating higher concentrations of UDMH in wastewater. Furthermore, these methods are mainly disadvantageous in that they generate NDMA, which is even more toxic than UDMH.[5] Recently, a series of new methods were developed for the degradation of UDMH. Smirnov *et al.*[6] studied the transformation mechanism of UDMH by catalytic combustion over Pt/SiO_2 catalyst at different temperatures, the UDMH decomposed by two-step oxidation. The residue consists mostly of condensed C≡N nitrile groups which totally block the platinum surface. However, it is not suitable for the purification of UDMH wastewater.

As an energy-efficient, green, and environmentally friendly technology, photocatalysis has a good application prospect in environmental pollution eliminated.[7] It is well known that titanium oxide (TiO_2) has been widely used due to its non-selectivity during the photocatalytic degradation of organic compounds, photocatalytic hydrogen production, organic synthesis, medical and health care, architectural coatings, and so on.[8] Nano TiO_2 is favored in practical research because of its good photoelectric properties due to its quantum yield.

---

[a] *Xi'an Research Inst. of Hi-Tech, Xi'an 710025, China. E-mail: 157771601@qq.com*
[b] *Engineering Quality Supervision Center, Beijing, 100142, China*

† Electronic supplementary information (ESI) available. See DOI: https://doi.org/10.1039/d2ra05953c

However, TiO_2 can only be activated under UV light due to its wide band gap (E_g, 3.0–3.2 eV). To overcome the drawbacks, there has been several strategies to modify TiO_2 including chemical (metal, non-metal doping and co-doping, coupled semiconductors) and morphological (higher surface area/porosity) techniques. Coupling TiO_2 with other narrow band gap semiconductors with matching band potentials to form heterojunction structures has been considered to improve its efficiency. The composite heterojunction system can be excited by visible light irradiation and can induce the efficient separation of photogenic e^-/h^+. A variety of composite materials have been reported, such as CdS/TiO_2,[9] Fe_2O_3/TiO_2,[10] ZnO/TiO_2,[11] $g\text{-}C_3N_4/TiO_2$,[12] and so on. In addition, the support with high specific surface area is also one of the effective ways to improve the photocatalytic activity. Huang *et al.*[13] synthesized TiO_2/SBA-15 catalysts with SBA-15 mesoporous silica as photocatalyst support, and optimized the photocatalytic removal efficiency of UDMH by adjusting the Si/Ti ratio. However, powdered TiO_2 is difficult to recycle for the next application and it would form secondary pollution. Therefore, this study of immobilized supported TiO_2 is of great significance for practical applications.

There are many immobilization technologies of TiO_2, which can be divided into physical deposition and chemical combination according to the way of binding with the substrate. Physical deposition type, such as dip-coating method,[14] electrospinning.[15] However, there was the problem of insufficient adhesion between catalyst and support. Chemical binding type, such as thermal spraying,[16] magnetron sputtering,[17] atomic layer deposition,[18] pulsed laser deposition,[19] micro-arc oxidation and other methods. There were deficiencies of complex equipment operation, high reaction temperature which was difficult to determine the best activity of anatase crystal. Chemical combination type, there were chemical vapor deposition,[20] liquid phase deposition,[21] electrophoretic deposition,[22] continuous ion layer adsorption reaction[23] and hydrothermal method,[24] the reaction temperature is relatively lower. Masuda had developed a two-step molding process for fabricating a nanohole array of anodic porous alumina,[25] and Pt and Au nanotube arrays were further obtained by electrodeposition. It could overcome the disadvantages of insufficient chemical and thermal stability and low mechanical strength. It has attracted extensive attention because of its rich pore structure, large specific surface area and high bonding strength. Certainly, TiO_2 nanotube arrays (TNAs) could be synthesized by anodic oxidation process,[26,27] which exhibiting highly photocatalytic oxidation activity and would be widely used in the field of photocatalysis, solar energy conversion, electrochromic.[28] Such as degradation of organic pollutants,[11] water oxidation, oxygen reduction,[24] photoelectrochemical sensor and photo fuel cell.[29] The anodic oxidation method is to form a regular tube array structure on the surface of pure metal by *in situ* current corrosion. Its morphology and photoelectric properties of TNAs were easily affected by composition of electrolyte, applied potential, the time of anodization, calcination temperature and others.[30,31] Especially, Das S. *et al.*[32] and Ai *et al.*[33] investigated the effect of temperature on the crystalline phase formation and composition of TNAs. The energetic alignment of the band edges of the rutile and anatase phases in the TNAs was very important to clarify the underlying mechanism and to design the high-performance photoelectrodes. However, there is still a lack of a research showed that various factors have a comprehensive impact on TNAs performance. Herein, the preparation technology of TNAs prepared by the anodic oxidation method and the test method of photoelectric properties were systematically studied for the first time by orthogonal experiment.

Currently, researchers paid more attention to the application of TNAs modification to improve photocatalytic properties.[8,34] The common modification methods include semiconductor composite, element doping, morphology control, *etc.* Because of the unique $6s^2$ electron of Bi element partially coincides with the O 2p orbital, which is beneficial to reduce the band gap of semiconductor material and respond to visible light.[35,36] Therefore, a series of Bi_2O_3 modified TNAs materials were prepared by electrodeposition method and applied to the degradation of UDMH wastewater. In comparison to the pure photocatalytic degradation of UDMH, a bias potential was applied to improve the separation efficiency of photogenerated carriers and the performance of photocatalysts.

2 Experiment

2.1 Reagents and instruments

UDMH (98%) was provided by the Rocket Force Propellant Analysis Center, NDMA (1000 mg L^{-1}) was purchased from O2si (USA), and FDMH (98%) was purchased from Aladdin Biochemical Technology Co., Ltd. Other reagents were analytically pure, and the experimental water was ultrapure water.

UPT-II-20T ultrapure water machine, IT6154 DC power, KB-12B high-temperature furnace, P4000A electrochemical workstation, *etc.* ECO ion chromatograph (IC), metrosep C4 cation column (4.0 mm × 150 mm), conductivity detector, ultimate 3000 high performance liquid chromatography (HPLC), Acclaim C18 reversed-phase column (4.6 mm × 250 mm × 5 μm), DAD-3000 detector.

2.2 Preparation of TNAs

High-purity titanium sheets (>99.99%) were cut into pieces of 1.5 cm × 4.5 cm, chemically polished with a mixture of 5% wt HNO_3 and 0.05% wt HF, and then ultrasonically treated with acetone, ethanol, and deionized water for 15 min, and dried with cold air. Dissolve F/Cl ion solute with water in 320 mL ethylene glycol (EG) in a certain proportion to form an electrolyte, and adjust the appropriate pH value of the solution, set anodic oxidation potential, with titanium as an anode, Pt as the counter electrode, for anodic oxidation film. And then the titanium sheet was take out and treated with ultrasonic oscillation in deionized water, 0.05% wt HF solution for 10–15 s, washed with deionized water, respectively, and dried with cold air. Finally, it was put into a high-temperature furnace, heated to 450–550 °C at a rate of 2 °C min^{-1}, calcined in air atmosphere for 4 h, and cooled with the furnace to obtain the sample TNAs.

The nine influencing factors of electrolyte composition, concentration of electrolyte, water content, pH, anodic oxidation potential, distance between electrodes, reaction temperature, reaction time, and calcination temperature, which were named factors A, B, C, D, E, F, G, H and I in order. The nine factors were used to design a 3-level orthogonal test with orthogonal table L27 (311). And the corresponding levels in order were: NaF, NH_4F, NH_4Cl, 0.1 mol L^{-1}, 0.2 mol L^{-1}, 0.3 mol L^{-1}, 1% vol, 3% vol, 5% vol, 5, 7, 9, 30 V, 40 V, 50 V, 2 cm, 3 cm, 4 cm, 25 °C, 30 °C, 35 °C, 30 min, 60 min, 90 min, 450 °C, 500 °C, 550 °C.

2.3 Preparation of TNAs/Bi_2O_3

1 mmol $Bi(NO_3)_3$ was dissolved in 1 ml of 34% nitric acid solution and then added to 100 ml of ethylene glycol to form a homogeneous electrolyte. The preparation process with the optimized photoelectric properties was obtained, and the modification of TNAs was carried out by electrochemical deposition of $Bi(NO_3)_3$. The optimized TNAs as the cathode, Pt as the anode, the potential was 6.0 V and the distance between electrodes was 4 cm, the deposition amount of Bi^{3+} was controlled by the reaction time (min). The TNAs/Bi_2O_3 samples were named as TNAs-1, TNAs-5 and TNAs-10 according to the deposition time. Following anneal it at the optimized temperature for 4 h with heating rate of 2 °C min^{-1} in muffle furnace. The experimental schematic diagram was shown in Fig. S1.†

2.4 Photoelectrochemical performance test

A three-electrode test system was constructed with a TNAs sample as the electrode, a Pt plate as the counter electrode, and an Ag/AgCl electrode as the reference electrode. 0.5 mol L^{-1} Na_2SO_4 solution as the electrolyte, the optical power of incident light at the working electrode position was 100 mW cm^{-2}, and the photoelectrochemical performance was evaluated with the photocurrent density i (mA cm^{-2}). I–t curves of the samples with different electrodeposition times were tested under repeated changes of light and dark conditions at 0.5 V (*vs.* ref. Ag/AgCl).

2.5 Evaluation of photocatalytic degradation towards UDMH wastewater

CEL-LAB500E 350 W xenon lamp with AM 1.5 filter was used to simulate sunlight as the catalytic light source, and the light power density was set to 100 mW cm^{-2}. The catalyst was applied to 40 ml of 100 mg L^{-1} UDMH wastewater. Prior to irradiation, dark experiments (adsorption) were carried out for 30 min to reach the adsorption equilibrium of UDMH with the catalyst.

The photocatalytic performance of the material was evaluated by degradation efficiency R and reaction kinetics of UDMH. The formula is as follows:

$$R = (C_0 - C_t)/C_0 \tag{1}$$

where C_0 is the initial concentration of UDMH, mg L^{-1}; C_t is the concentration of UDMH in the wastewater at the time of photocatalytic reaction t, mg L^{-1}. The general photocatalyst degradation of organic pollutants is a pseudo primary kinetic reaction with the following equation:

$$\ln \frac{C_0}{C_t} = kt \tag{2}$$

where k is the primary kinetic reaction rate constant, h^{-1} or min^{-1}; t is the time for photocatalytic degradation of UDMH. UDMH in wastewater was detected with the ion chromatography method,[37] and the intermediate products of wastewater degradation, NDMA and FDMH were detected with HPLC.[4]

2.6 Detection of free radical

According to the process of photocatalytic degradation of organic matter was mainly caused by the direct oxidation of organic pollutants by photogenerated h^+/e^- pairs, or the reaction with surface adsorbed oxygen (O_2), H_2O/OH^- to generate superoxide radicals ($^{\bullet}O_2^-$), hydroxyl radicals ($^{\bullet}OH$) and other active radicals indirectly involved in the reaction. For semiconductor materials, when the conduction band (CB) of the photocatalytic material is more negative than the redox potential of $O_2/^{\bullet}O_2^-$ (−0.046 eV, *vs.* NHE), the photogenerated electrons (e^-) could react with O_2 to form $^{\bullet}O_2-$, when the redox potential of VB is more positive than that of $H_2O/^{\bullet}OH$ (2.4 eV, *vs.* NHE), the photogenerated holes (h^+) could oxidize H_2O/OH^- to form $^{\bullet}OH$.[38] Simultaneously, the more O_2 on the surface of the catalysts, the more conducive to generation $^{\bullet}O_2^-$.

The trapping agent is added to preferentially interact with the free radicals to form a stable molecular morphology. The mechanism of photocatalytic degradation was analyzed by its effect on UDMH degradation. Herein, 1 mmol L^{-1} isopropanol (IPA), *p*-benzoquinone (PBQ), ethylenediamine tetraacetic acid disodium salt (EDTA) and carbon tetrachloride (CTC) were used as quenching agents for $^{\bullet}OH$, $^{\bullet}O_2^-$ h^+, and e^-, respectively. The effects of active species produced by different materials in the photocatalytic process on the degradation of UDMH wastewater were investigated. The process of UDMH wastewater degradation without a capture agent was used as a blank, and other conditions were consistent with previous ones.

3 Result and discussion

3.1 Optimization of TNAs preparation process

3.1.1 Analysis of morphology structure. The microstructure of the samples was observed by SEM characterization. As shown in Fig. S2,† the obvious TNAs structure can be observed in the anodic oxidation samples obtained from the electrolyte containing F^-, the samples from 1 to 18, which were prepared withNaF and NH_4F electrolytes. While the samples from 19 to 27 were prepared with NH_4Cl electrolyte showed irregular and disordered corrosion pore structure, and there was no obvious nanotube array morphology. The corrosion reaction of NH_4Cl to Ti was violent, which was easy to form macroporous structure. This is because substances with strong oxidation activity are generated in the electrochemical reaction process, such as Cl_2, ClO^-, *etc.* Which result in the rapid corrosion process of Ti. In addition, unstable $TiCl_4$ may be formed in the reaction process and react with H_2O quickly to decompose into TiO_2 particles. Fluoride electrolyte had better controllability for the corrosion process of Ti sheet.

It was found that electrolyte concentration, water content and pH were positively correlated with corrosion. Especially, in alkaline conditions, the nanotube structure was almost invisible on the surface of the material. The corrosion process is relatively stable under neutral conditions, and the morphology is easier to control. The anodic oxidation potential, distance between electrodes and reaction temperature mainly affected the degree of corrosion and the formation rate of nanotubes. The reaction time mainly affected the length and pore size of nanotubes. Calcination temperature mainly affects the crystal structure of TiO_2, the main crystal form is anatase from 450 °C to 550 °C.

3.1.2 Photoelectrochemical performance analysis. The photoelectrochemical activity of the material was visually analyzed by the mean and range of the orthogonal test results, as shown in Fig. 1(a) and Table S1† Which were used as an indirect evaluation basis for the photocatalytic activity of the material. The effect curve of mean value optimization method was shown in Fig. 1(b). The higher the mean value, the better the photoelectric performance.

The optimal process conditions were as follows: the electrolyte was 0.2 mol L^{-1} NaF solution, the water content was 3% vol, pH = 7, the anodic oxidation potential was 40 V, distance between electrodes was 4 cm, the reaction time was 90 min, and following 450 °C calcination annealing. It can be seen from the range analysis that the influence order of 9 factors on the photocurrent density of TNAs was: anodic oxidation potential < distance between electrodes < calcination temperature < electrolyte solute < water content of electrolyte < anodic oxidation temperature < pH < anodic oxidation time < solute concentration.

According to the experimental results, the morphology and structure of the orthogonal optimization results are shown in Fig. 2(a). The nanotube length and diameter of the TNAs nanotubes were 12.21 μm, 103 nm, respectively. However, due to the instability of the mechanical structure caused by the long nanotube, it was easy to shed due to external force. Anodic oxidation time is the main reason for the growth of nanotubes, therefore, adjusted the anodic oxidation time to the second level of 60 min. After re-optimization of the sample nanotube length dropped to 7.67 μm, the film and the substrate binding degree increased significantly, and the diameter change was not obvious, as shown in Fig. 2(b). Fig. 2(c) is EDS spectrum of the re-optimized TNAs, which contained Ti and O elements. Fig. 2(d) is the XRD spectrum. It can be observed that the more obvious diffraction peaks of 25.26°, 37.78°, and 48.02° were (101), (004) and (200) crystal plane diffraction peaks of anatase TiO_2 (PDF # 73-1764). While the diffraction peaks of 35.06°, 40.25°, and 52.96° were the (100), (101) and (102) crystal plane characteristic diffraction peaks of Ti (PDF # 89-5009). Furthermore, there were overlapping diffraction peaks of TiO_2 and Ti at 38.4°, 62.86°, 70.82° and 76.12°, respectively.

3.2 Modification of TNAs by Bi_2O_3

3.2.1 The structure characterizations. The substrate was prepared under optimized parameters and modified by electrodeposition of Bi^{3+}. The SEM images of the samples with different deposition time are shown in Fig. 3. The nanotube array structure of the substrate material was neat. As the deposition time increases, the particles of Bi_2O_3 deposited on the surface of TNAs gradually increased. The particle size on the surface of TNAs-1 was about 100 nm and evenly distributed. When the deposition time reached 5 min, the Bi_2O_3 particles on the surface of TNAs-5 increased, the distribution density increases uniformly, and the size of a small amount of particles increased slightly. When the deposition time reached 10 min, the Bi_2O_3 particles grew into a flower-like structure, the size increased significantly, and basically covered the surface of TNAs. It could be seen from the EDS spectrum (TNAs-10) analysis that the surface of the material mainly contains three elements: Bi, Ti, and O.

XRD characterization results showed that the crystal parameters of TNAs did not change significantly after Bi_2O_3 loading modification, as shown in Fig. 4. The diffraction peaks at 35.17°, 40.25° and 53.09° correspond to the (100), (101) and (102) planes of Ti substrate, respectively. 25.37°, 37.05°, 37.91°, 38.67°, 48.16°, 54.05°, 55.20°, 62.87° and 75.28° correspond to

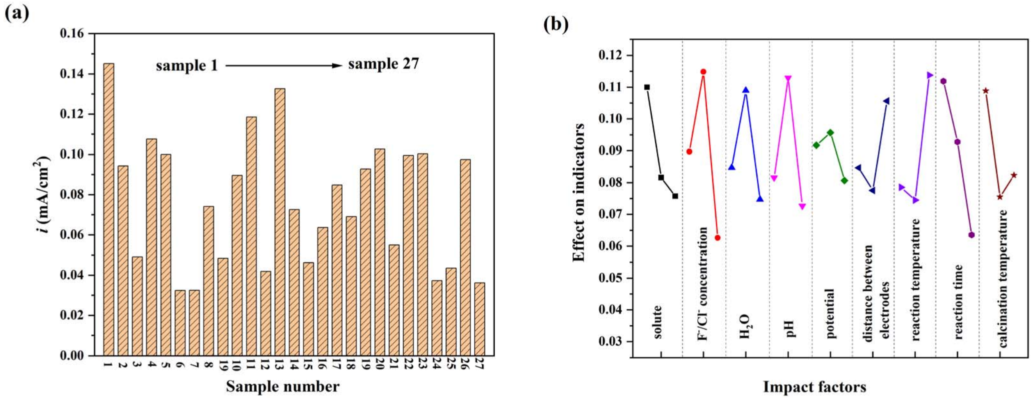

Fig. 1 (a) Light response current density and (b) effect curve of TNAs orthogonal test samples.

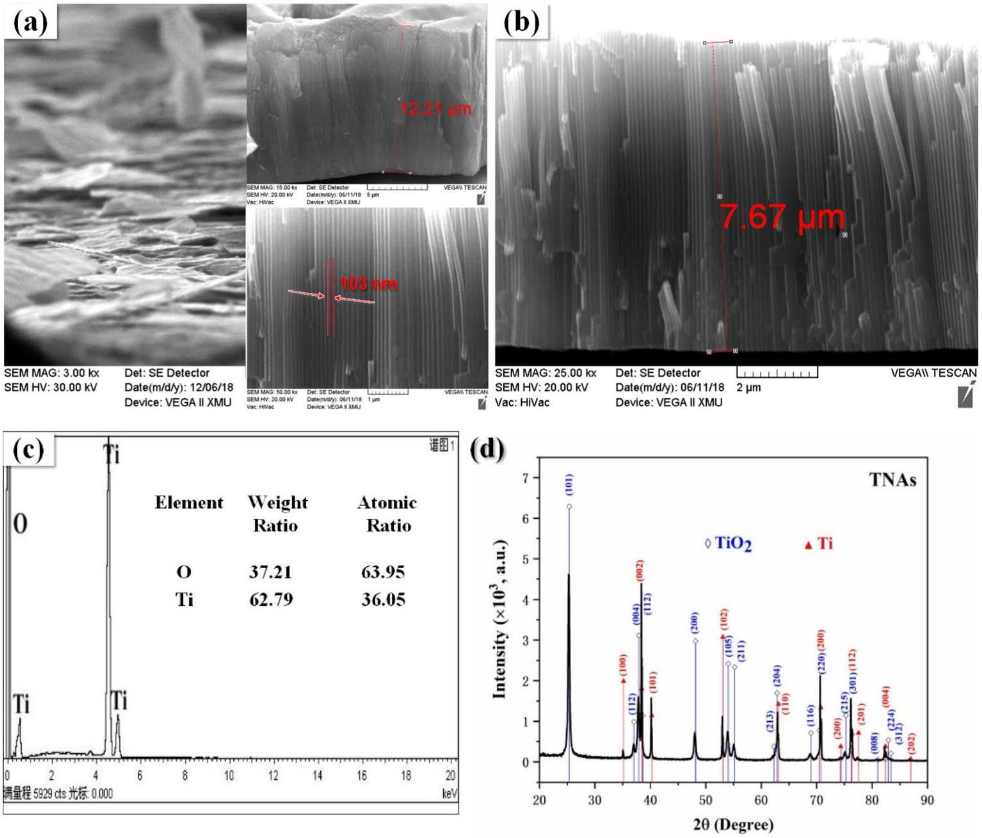

Element	Weight Ratio	Atomic Ratio
O	37.21	63.95
Ti	62.79	36.05

Fig. 2 Orthogonal optimization of TNAs (a) SEM and re-optimized (b) SEM, (c) EDS, (d) XRD.

the (101), (103), (004), (112), (200), (105), (211), (204) and (215) planes of TiO_2 respectively. Different from TNAs and TNAs-1, TNAs-5 showed weak diffraction peaks at 27.9°, 32.84° and 46.18°, while TNAs-10 shows obvious diffraction peaks, which belonged to (201), (220), and (222) planes of Bi_2O_3, respectively. This showed thatTiO_2 on the TNAs substrate was mainly anatase, and composite Bi_2O_3 was obtained by electrodeposition on its surface.

A typical XPS survey scan for TNAs and TNAs-10 to investigate the chemical valence states of surface elements of this sample, as shown in Fig. S3.† The full spectra showed that TNAs mainly contains Ti, O and C elements (Fig. S3a†), and TNAs-10 was composed of Ti, Bi and O elements (Fig. S3b†), indicating that the Bi-contained species have been introduced into the TNAs composite. It is noted that the C element is originated from the contaminants during the testing process (Fig. S3c†). In Fig. S3d,† the binding energies of O 1s located at 528.3 and 530.5 eV are assigned to lattice oxygen (O^{2-} of Ti–O/Bi–O bond) and surface hydroxyl oxygen (OH^-). As displayed in Fig. S3e,† the double peaks with binding energies at 457.3 eV and 463.0 eV on the pure TiO_2 correspond to Ti $2p^{3/2}$ and Ti $2p^{1/2}$ in the form of Ti^{4+}.[39] It is noted that a is enhanced and broadened peak can be observed on TNAs-10 min at 464.8 eV which belonged to the overlapping peak of Bi 4d and Ti $2p^{1/2}$. The Bi $4f^{7/2}$ and Bi $4f^{5/2}$ doublet core peaks are observed at 157.8 eV and 163.1 eV (Fig. S3f†), indicating that Bi was existed in the form of Bi^{3+}.[35]

3.2.2 UV-vis analysis. As the amount of Bi_2O_3 increased, the intensity of TNAs materials absorbing visible light increased gradually. When the electrodeposition time increased to 10 min, the increasing trend of visible light absorption decreased, indicating that the loading of Bi_2O_3 tends to be optimized, as shown in Fig. 5(a). Interestingly, at <420 nm, Bi_2O_3 can increase the visible light response intensity of TNAs. While at >420 nm, it is subject to the synergistic effect of TiO_2 and Bi_2O_3, which can simultaneously increase the response intensity of both to visible light. The band gap of the semiconductor material was further estimated, as shown in Fig. 5(b). The band gap of the unmodified TNAs substrate was about 3.00 eV. It showed that the nanotube array structure could reduce the band gap of TiO_2 (3.20 eV). As the amount of Bi_2O_3 increased, the band gap gradually decreased, indicating that the modification of Bi_2O_3 ($E_g = 2.8$ eV) was beneficial to reduce the band gap of the material, and the band gap of TNAs-10 decreased to 1.86 eV.

3.2.3 Photoelectrochemical analysis. The photocurrent results for the samples were shown in Fig. 6(a), photocurrent changed obviously with light irradiation, indicating that the electrode material was very sensitive to light. The photocurrent densities of TNAs, TNAs-1, TNAs-5 and TNAs-10 were 0.09 mA cm^{-2}, 0.13 mA cm^{-2}, 0.21 mA cm^{-2} and 0.26 mA cm^{-2}, respectively. The photocurrent density of TNAs-10 was about three times that of TNAs, indicating that the loading

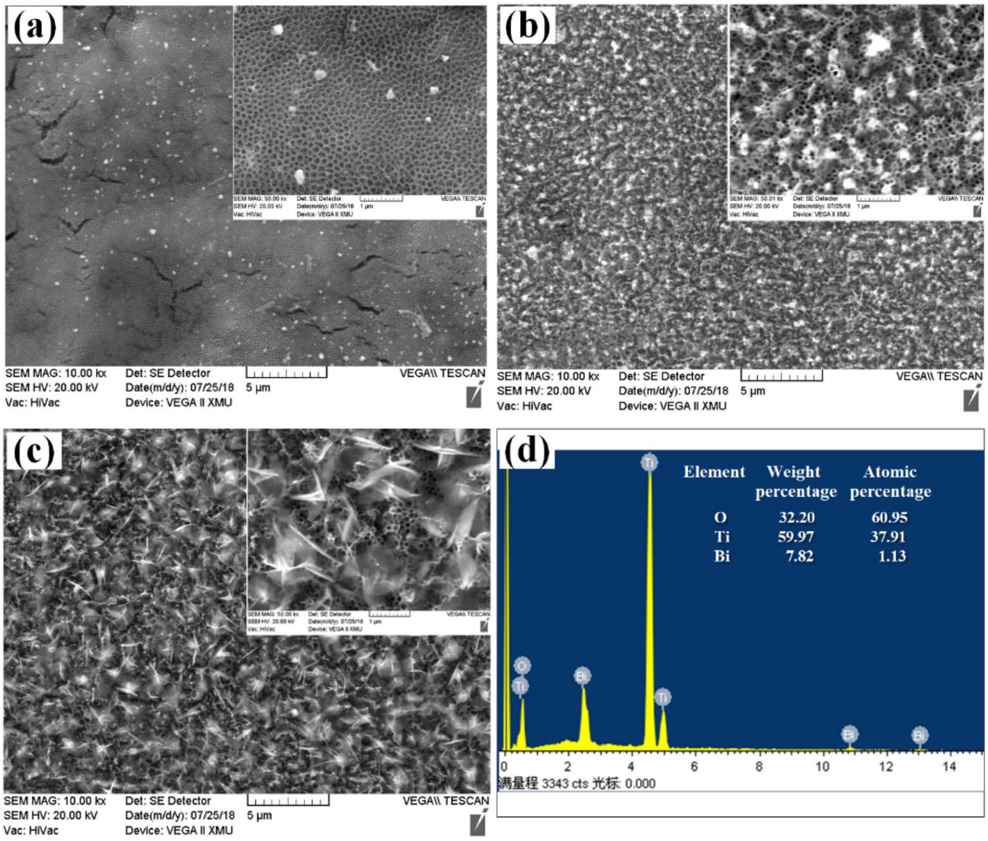

Element	Weight percentage	Atomic percentage
O	32.20	60.95
Ti	59.97	37.91
Bi	7.82	1.13

Fig. 3 SEM of different electrodeposition time (a) TNAs-1, (b) TNAs-5, (c) TNAs-10 and (d) EDS.

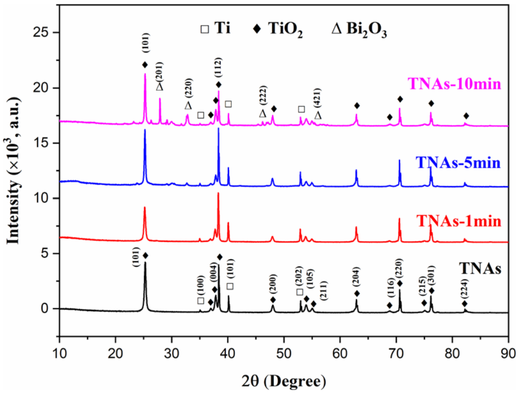

Fig. 4 XRD of TNAs/Bi_2O_3.

modification of Bi_2O_3 improved the yield and separation efficiency of photogenerated carriers and also showed that the photoelectric activity of the samples were improved.

To further reveal the e^-/h^+ recombination in the samples, the PL spectrum was obtained, and the results were shown in Fig. 6b. The PL emission spectra were measured at an excitation wavelength of 350 nm. The higher the recombination rate, the stronger the fluorescence emission. The fluorescence emission peak intensity of the samples at approximately 465 nm gradually decreased with the increase of Bi_2O_3 loading, indicating that the modification of Bi_2O_3 was helpful to reduce the recombination probability of photogenerated carriers and improve the quantum efficiency of the material.

3.3 Photocatalytic performance

2.3.1Effect of Bi_2O_3 modification on photocatalytic activity. The photocatalytic activity of catalysts was evaluated by the degradation of UDMH wastewater under simulated solar light irradiation, the performance was shown in Fig. 7. Prior to irradiation, dark experiments (adsorption) were carried out for 30 min to reach the adsorption equilibrium, the adsorption of UDMH was 0.3%–1.8%, mainly contributed by the pore structure of the nanotube array with a high specific surface area. With the extension of illumination time, the degradation rate of UDMH increased. After irradiation for 10 h, the pure TNAs displayed the degradation rate of 33.09%. While the degradation rate on the samples of TNAs modified by Bi_2O_3 were significantly improved. The degradation rates of UDMH wastewater on the TNAs-1, TNAs-5, and TNAs-10 were 72.47%, 85.82%, and 89.14%, respectively. The degradation rate of UDMH on TNAs-10 was 2.69 times of that on the pure TNAs, which was consistent with the photocurrent density test. After evaluating by first-order kinetic model, the reaction rate constants of UDMH wastewater degradation on TNAs, TNAs-1, TNAs-5, and TNAs-10 were 0.041 h^{-1}, 0.125 h^{-1}, 0.193 h^{-1}, and 0.215 h^{-1}, respectively, illustrating that the photocatalytic

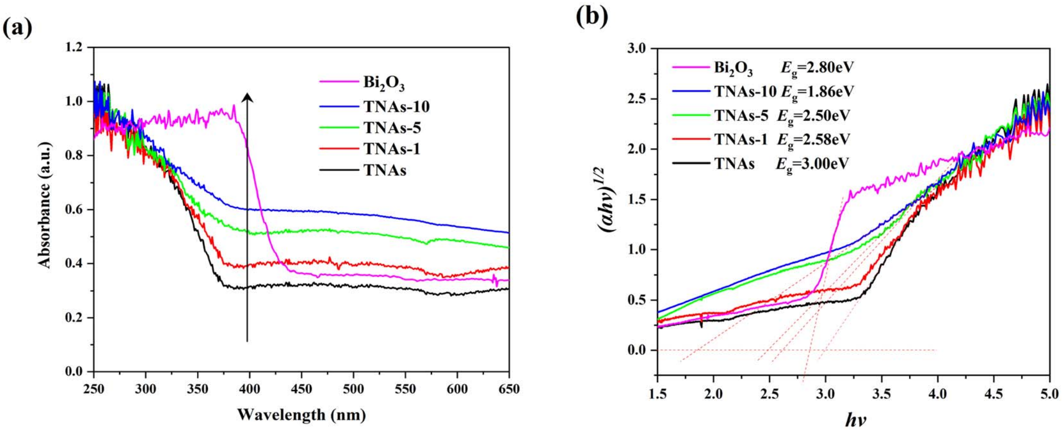

Fig. 5 (a) UV-vis absorption spectra and (b) band gap estimation curves modified by different electrodeposition time.

activity can be enhanced significantly when TNAs was modified by an appropriate amount of Bi_2O_3.

3.3.2 Effect of bias voltage on photocatalytic activity. According to the characteristic that the electric field inside the heterojunction can improve the separation efficiency of photogenerated carriers, an auxiliary electric field was established with TNAs-10 as photo anode and graphite as cathode. Photogenerated e^-/h^+ pairs would be accelerated to separate by a bias potential, which improving the photocatalytic activity, denoted as TNA-10 (bias). Since the redox potential of superoxide radical ($^{\bullet}O_2-$) is -0.33 V (*vs.* SHE), a higher bias potential was easy to reduce the active substance to O_2 during the photocatalytic process. Therefore, the bias potential of the photocatalytic anode was set to +0.3 V (*vs.* open circuit potential).

The bias potential significantly improved the degradation efficiency of UDMH wastewater, as shown in Fig. 8. The degradation rate of UDMH on TNAs-10 (bias) was 94.03% in 6 h, and UDMH was completely degraded in about 8 h. It performed better than TNAs-10 with the rate of 89.14% (10 h), as shown in Fig. 8a. Evaluating by pseudo-first-order kinetic module, the degradation rate constant of UDMH wastewater on TNAs-10 was 0.215 h^{-1}, and the degradation rate of UDMH wastewater on TNAs-10 (bias) was exponentially distributed, as shown in Fig. 8b. Thus, the bias potential played an important role in improving the photocatalytic activity.

3.3.3 Degradation of FDMH and NDMA. Simultaneously, we studied the changes of FDMH and NDMA during the photocatalytic degradation of UDMH, as shown in Fig. S4.† The results revealed that the FDMH increased first and then decreased, of which the content were highest in the second hour and completely degraded in the ninth hour. NDMA presented the same trend, of which the content reached the highest in third hour and completely degraded in the tenth hour. Compared with TNAs-10, the maximum contents of FDMH and NDMA on TNAs-10 (bias) reached earlier, and the degradation were completed 1–2 hours earlier, indicating that the bias potential could accelerate the photocatalytic degradation of UDMH.

In addition, the higher generation of FDMH than NDMA was due to the priority of FDMH generation is higher in UDMH degradation process.[40]. Finally, FDMH and NDMA were

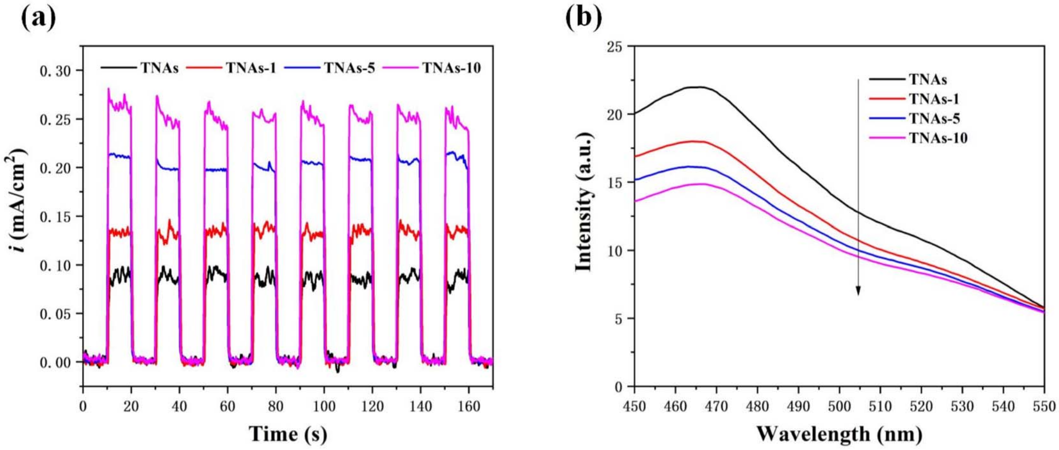

Fig. 6 Electrical tests on catalyst samples. (a) Photocurrent densities with the potential of +0.5 V (*vs.* ref. Ag/AgCl), (b) PL spectrum.

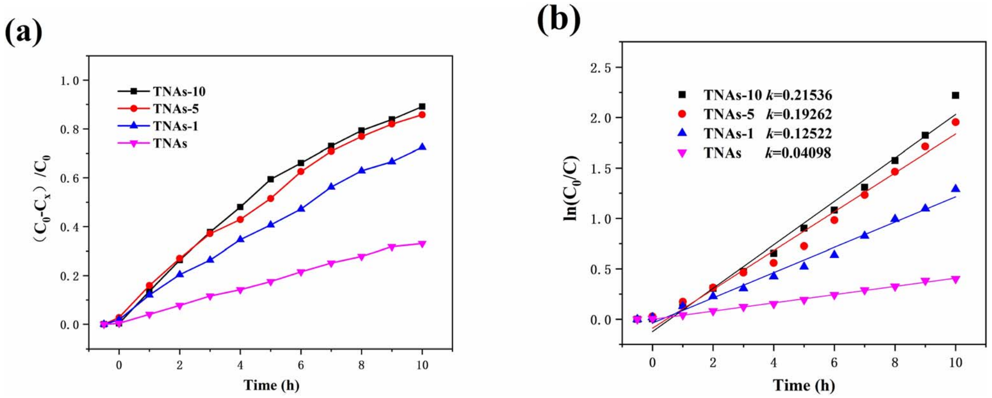

Fig. 7 (a) Degradation rate of UDMH, (b) the pseudo-first-order kinetics of UDMH removal rate.

completely degraded, indicating that both TNAs-10 and TNAs-10 (bias) could realize non-toxic treatment of UDMH.

3.3.4 Photocatalytic stability analysis. The photocatalytic performance of TNAs-10 and TNAs-10 (bias) in five cycles were shown in Fig. S5.† At the end of each cycle, the samples were soaked in water for 10 min, washed, and dried at 60 °C. It can be seen from the diagram that the photocatalytic activity of TNAs-10 remained basically unchanged. After five cycles, the photocatalytic degradation efficiency of UDMH wastewater on TNAs-10 changed from 89.14% to 86.59%, only reduced by 2.55%, which on TNAs-10 (bias) decreased from 99.8% to 89.04%, with a decrease of 10.76%. It can be found that the external bias voltage is beneficial to improve the photocatalytic activity of TNAs-10. The degradation efficiency of UDMH wastewater gradually decreased with the increase of cycle times. In order to analyse the causes of deactivation, the crystalline composition and morphology of the sample after stability test were evaluated by SEM and XRD, as shown in Fig. S7 and S8.† After stability testing, lumpy deposits appeared on the surface of the samples, sealing the nanotubes; the formerly regular Bi_2O_3 particles reorganised into piles of fine particles, which may account for the deactivation of Bi_2O_3. Further analysis by XRD characterisation revealed that most of the diffraction peaks of Bi_2O_3 disappeared and only the faint diffraction peaks at 32.46° (220), 46.18° (222) could be observed. It may be that the electrochemical redox reaction of the external electric field destroyed the structure and composition of the photocatalyst. Meanwhile, the external particle impurities were deposited and covered on the surface of photocatalyst by the electrostatic field, thus reducing the photocatalytic active spots.

3.4 Mechanism of photocatalytic degradation

3.4.1 Active species capture experiments. The comparative decay of UDMH with and without scavengers in photocatalysis processes were illustrated in Fig. S6.† The removal rate of UDMH without scavengers on TNAs-10 and TNAs-10 (bias) were 89.14% and 99.11%, respectively. In addition, with IPA, PBQ, and EDTA, UDMH removal displayed values of 54.58%, 64.28%, 51.52% on TNAs-10 and 45.24%, 68.32%, 56.43% on TNAs-10 (bias), respectively. However, the degradation efficiency of UDMH slightly reduced with CTC, of which were 85.85% and 88.32%. This result confirmed that, during UDMH degradation in the TNAs-10 and TNAs-10 (bias) system, the amount of reactive species were $^{\cdot}OH > h^+ > {^{\cdot}O_2}^- > e^-$ and $h^+ > {^{\cdot}OH} > {^{\cdot}O_2}^- > e^-$, respectively. Differences in inhibition produced by these two system indicated that $^{\cdot}OH$ played a more important role in

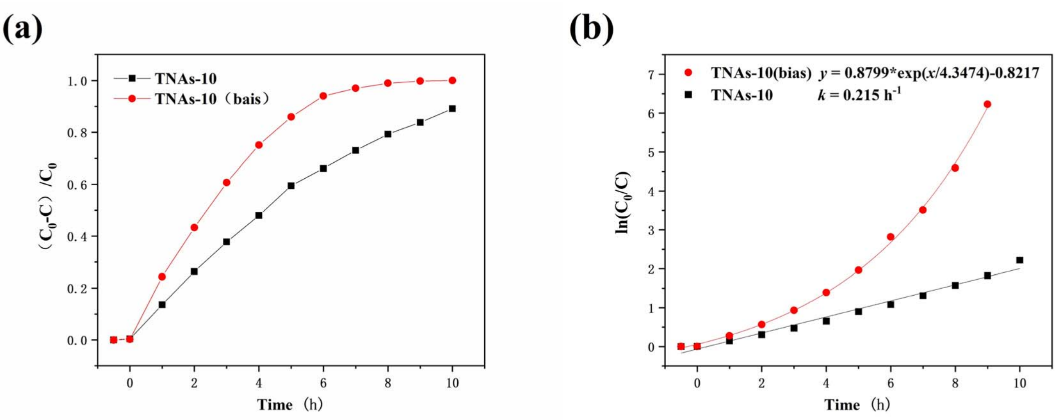

Fig. 8 (a) Degradation of UDMH on TNAs-10 and TNAs-10 (bias) and (b) kinetic fitting curve.

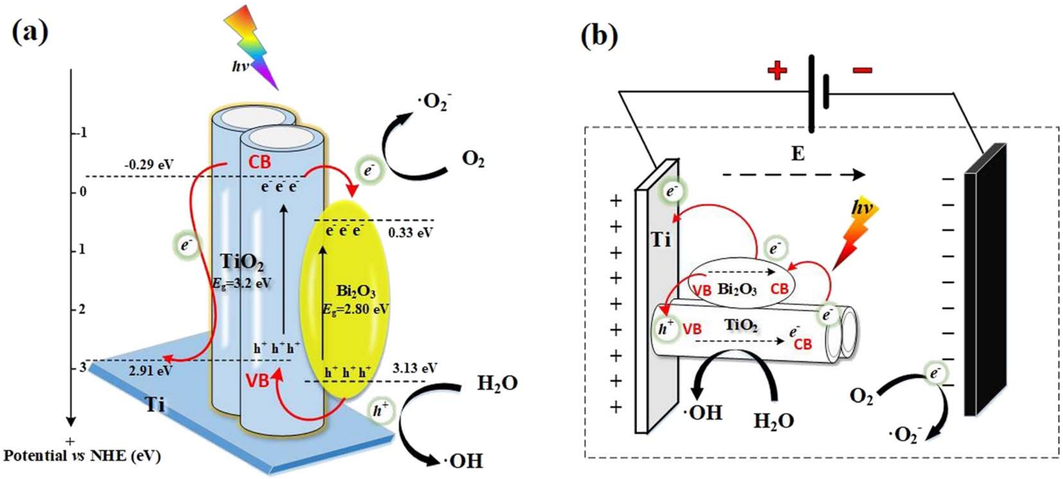

Fig. 9 Mechanism of photocatalytic degradation: (a) TNAs-10, (b) TNAs-10 (bias).

TNAs-10 and h^+ in TNAs-10 (bias). When PBQ was used to capture $^{\bullet}O_2^-$ during the photocatalytic degradation of UDMH process, the degradation rate were reduced remarkably, suggesting that $^{\bullet}O_2^-$ was formed during UDMH treatment. It was due to the position of photocatalytic active center had been changed in the external electrostatic field. Simultaneously, it was found that TNAs-10 (bias) with applied bias potential displayed a higher degradation rate of UDMH wastewater than TNAs-10, which was due to the separation of photogenerated carriers is accelerated in the applied electric field and produces more active species to participate in the reaction.

3.4.2 Schematic of photocatalytic degradation of UDMH in theory. The semiconductor heterojunction is formed by depositing Bi_2O_3 on the surface of TNAs. The band-gap energy of TiO_2 and Bi_2O_3 adopts 3.2 eV, 2.80 eV, respectively. The CB and valence band (VB) potentials of TiO_2 at the point of zero charge are −0.29 eV and 2.91 eV, respectively, and which of Bi_2O_3 are 0.33 eV and 3.13 eV,[4,41] as shown in Fig. 9a. The Fermi energy level of TiO_2 approached to the CB belong to the intrinsic n-type semiconductor, which of Bi_2O_3 approached to the VB belong to the intrinsic p-type semiconductor. The Fermi level of the Bi_2O_3 is lower than that of the TiO_2. When the two types of semiconductor materials were combined together, the Fermi level of Bi_2O_3 was moved up and that of TiO_2 was moved down along until the Fermi levels of Bi_2O_3 and TiO_2 attained a same value. Meanwhile, the whole energy band of Bi_2O_3 was raised up while that of TiO_2 was lowered down, as a result, the CB edge of p-type Bi_2O_3 is higher than that of n-type TiO_2. A p–n heterojunction was formed at the interface between Bi_2O_3 and TiO_2. Thus an internal electric field from n-type TiO_2 to p-type Bi_2O_3 was established. Which facilitated the rapid transfer of photogenerated carriers, thereby improving the separation efficiency of photogenerated carriers. Due to the inconsistent deposition time of each point on the surface of TNAs, quantum-sized Bi_2O_3 (<50 nm) appeared on the surface of TNAs. Quantum-sized Bi_2O_3 could trapped photogenerated electrons, and then reduced the recombination efficiency of photogenerated carriers. In addition, the energy band of quantum-sized Bi_2O_3 could be tuned by the quantum confinement effect,[42] which could also promote the separation of carriers.

In the presence of visible-light radiation, only Bi_2O_3 can be excited to generate h^+/e^- pairs. The e^- in the VB of Bi_2O_3 was excited to the CB, then further promoted by the built-internal electric field and easily transferred to that of TiO_2, and reacts with adsorbed oxygen (O_2) to form $^{\bullet}O_2^-$. While the generated h^+ remain in the VB of Bi_2O_3. As a result, the photogenerated h^+/e^- can be separated effectively, leading to the lifetime of the charge carriers can be effectively prolonged. Some of the photogenerated h^+ retained in the VB reacted with H_2O *in situ* to form $^{\bullet}OH$, and the others participated in the degradation of UDMH. It can be seen from the free radical capture experiment that the good conductivity of the Ti substrate enhanced the transfer of e^-, result in producing more $^{\bullet}O_2^-$ to participate in the photocatalytic degradation of UDMH. The main active species are still h^+ and $^{\bullet}OH$.

Interestingly, when the bias potential is applied, the degradation of UDMH by TNAs-10 (bias), $^{\bullet}OH$ is significantly increased. This probably occurred because the anode can also produce h^+ to react with H_2O to form $^{\bullet}OH$ with the action of an applied electric field. When the photocatalytic electrode is excited by light, the external electrostatic field accelerated the separation of photogenerated carriers, and the photogenerated e^- flowed along the external circuit to the cathode. Meanwhile, it reacted with the adsorbed oxygen (O_2) to form $^{\bullet}O_2^-$ and further to degrade UDMH. However, it would be limited by the small amount of oxygen in the water environment. The photoanode material retained a large amount of h^+, which directly oxidizes UDMH or reacts with H_2O to generate $^{\bullet}OH$, as shown in Fig. 9(b).

4 Conclusion

A series of TNAs film with anatase structures were fabricated *via* electrochemical anodization of high purity Ti foil. The nine factors affecting anodic oxidation were optimized by orthogonal experiment. TNAs were modified by electrodeposition of Bi_2O_3, and the degradation effect of UDMH wastewater was improved by the bias voltage. The main conclusions are as follows:

(1) The influence sequence of 9 factors on the photocurrent density of TNAs was as follows: anodic oxidation potential < distance between electrodes < calcination temperature < electrolyte solute < water content of electrolyte < anodic oxidation temperature < pH < anodic oxidation time < solute concentration. Optimal condition parameters were: 0.2 mol L^{-1} NaF, 3% vol H_2O, electrolyte with pH of 7, oxidation voltage of 40 V, electrode spacing of 4 cm, reaction for 60 min at 25 °C water bath.

(2) Bi_2O_3 modified TNAs films were obtained by electrodeposition. The degradation of UDMH in different TNAs/Bi_2O_3–based processes were evaluated and compared. The degradation followed the pseudo-first-order reaction kinetics model. The degradation rate of UDMH wastewater by TNAs-10 within 10 h was 89.14%, which was 2.69 times of that on the pure TNAs. The reaction rate constant was 0.215 h^{-1}.

(3) A bias potential of +0.3 V (*vs.* open circuit potential) was applied to the TNAs-10. The degradation rate of UDMH was significantly enhanced on the TNAs-10 (bias) process as compared to the TNAs-10 process. The degradation rate of UDMH wastewater on TNAs-10 (bias) exhibited an exponential distribution. The bias potential plays played an important role in promoting the photocatalytic degradation activity. UDMH and the toxic by-products FDMH, NDMA were completely degraded in 8 h. The results presented herein will provide innovative directions, valuable information and reference for effective removal of UDMH in water.

Prime novelty statement

Nine factors affecting anodic oxidation have been systematically optimised and results obtained using orthogonal experiments. The influence sequence of 9 factors on the photocurrent density of TNAs was as follows: anodic oxidation potential < distance between electrodes < calcination temperature < electrolyte solute < water content of electrolyte < anodic oxidation temperature < pH < anodic oxidation time < solute concentration. For the first time, bias potential photocatalysis was adopted, which improved the separation efficiency of photogenerated electron–hole pairs and the degradation efficiency of UDMH wastewater. The results provide a promising way for preparation of catalyst and degradation of UDMH.

Conflicts of interest

There are no conflicts to declare.

References

1 F. Chen, F. Wang, Q. Li, *et al.*, Effect of support (Degussa P25 TiO_2, anatase TiO_2, γ-Al_2O_3, and AlOOH) of Pt-based catalysts on the formaldehyde oxidation at room temperature, *Catal. Commun.*, 2017, **99**, 39–42.

2 A. L. Milyushkin, K. P. Birin, D. D. Matyushin, *et al.*, Isomeric derivatives of triazoles as new toxic decomposition products of 1,1-dimethylhydrazine, *Chemosphere*, 2019, **217**, 95–99.

3 C. Hu, Y. Zhang, Y. Zhou, *et al.*, Unsymmetrical dimethylhydrazine and related compounds in the environment: recent updates on pretreatment, analysis, and removal techniques, *J. Hazard. Mater.*, 2022, **432**, 128708.

4 F. Zhou and X. Ren, Reversible photochromic photocatalyst $Bi_2O_3/TiO_2/Al_2O_3$ with enhanced visible photoactivity: application toward UDMH degradation in wastewater, *J. Environ. Sci. Health, Part A: Toxic/Hazard. Subst. Environ. Eng.*, 2020, **55**(3), 239–255.

5 M. Liang, W. Li, Q. Qi, *et al.*, Catalyst for the degradation of 1,1-dimethylhydrazine and its by-product *n*-nitrosodimethylamine in propellant wastewater, *RSC Adv.*, 2016, **6**(7), 5677–5687.

6 A. V. Smirnov, P. A. Kots, M. A. Panteleyev, *et al.*, Mechanistic study of 1,1-dimethylhydrazine transformation over Pt/SiO_2 catalyst, *RSC Adv.*, 2018, **8**(64), 36970–36979.

7 K. Qi, B. Cheng, J. Yu, *et al.*, A review on TiO_2-based z-scheme photocatalysts, *Chin. J. Catal.*, 2017, **38**(12), 1936–1955.

8 A. Kumar, P. Choudhary, A. Kumar, *et al.*, Recent advances in plasmonic photocatalysis based on TiO_2 and noble metal nanoparticles for energy conversion, environmental remediation, and organic synthesis, *Small*, 2022, **18**(1), 2101638.

9 X. Gao, X. Liu, X. Wang, *et al.*, Photodegradation of unsymmetrical dimethylhydrazine by TiO_2 nanorod arrays decorated with Cds nanoparticles under visible light, *Nanoscale Res. Lett.*, 2016, **11**(1), 496.

10 M. M. Mohamed, W. A. Bayoumy, M. E. Goher, *et al.*, Optimization of α-Fe_2O_3@Fe_3O_4 incorporated N-TiO_2 as super effective photocatalysts under visible light irradiation, *Appl. Surf. Sci.*, 2017, **412**, 668–682.

11 J. You, L. Zhang, L. He, *et al.*, Photocatalytic degradation of methyl orange on ZnO–TiO_2/SO_4^{2-} heterojunction composites, *Opt. Mater.*, 2022, **131**, 112737.

12 J. Liu, B. Cheng and J. Yu, A new understanding of the photocatalytic mechanism of the direct z-scheme g-C_3N_4/TiO_2 heterostructure, *Phys. Chem. Chem. Phys.*, 2016, **18**(45), 31175–31183.

13 Y. Huang, Y. Jia, R. Hou, *et al.*, Photocatalytic degradation of unsymmetrical dimethylhydrazine on TiO_2/SBA-15 under 185/254 nm vacuum-ultraviolet, *RSC Adv.*, 2021, **11**(39), 24172–24182.

14 H. K. Hakki, S. Allahyari, N. Rahemi, *et al.*, Surface properties, adherence, and photocatalytic activity of sol–gel dip-coated TiO_2-ZnO films on glass plates, *C. R. Chim.*, 2019, **22**(5), 393–405.

15 T. Istirohah, S. Wihdatul Himmah and M. Diantoro, Fabrication of aligned PAN/TiO_2 fiber using electric electrospinning (ees), *Mater. Today: Proc.*, 2019, **13**, 211–216.

16 I. D. Utu, G. Marginean, I. Hulka, *et al.*, Properties of the thermally sprayed Al_2O_3-TiO_2 coatings deposited on titanium substrate, *Int. J. Refract. Met. Hard Mater.*, 2015, **51**, 118–123.

17 J. A. P. Nuñez, H. S. Salapare, M. M. S. Villamayor, *et al.*, Antibacterial efficiency of magnetron sputtered TiO_2 on poly(methyl methacrylate), *Surf. Interfaces*, 2017, **8**, 28–35.

18 F. Dvorak, R. Zazpe, M. Krbal, *et al.*, One-dimensional anodic TiO_2 nanotubes coated by atomic layer deposition: towards advanced applications, *Appl. Mater. Today*, 2019, **14**, 1–20.

19 I. Olvera-Rodríguez, R. Hernández, A. Medel, *et al.*, TiO_2/Au/TiO_2 multilayer thin-film photoanodes synthesized by pulsed laser deposition for photoelectrochemical degradation of organic pollutants, *Sep. Purif. Technol.*, 2019, **224**, 189–198.

20 L. Weihao, C. Shengnan, W. Jianxun, *et al.*, Study on structural, optical and hydrophilic properties of FTO/TiO_2 tandem thin film prepared by aerosol-assisted chemical vapor deposition method, *Surf. Coat. Technol.*, 2019, **358**, 715–720.

21 C. Xu, Y. Zhong, Y. Zheng, *et al.*, Micromixing-assisted preparation of TiO_2 films from ammonium hexafluorotitanate and urea by liquid phase deposition based on simulation of mixing process in t-shaped micromixer, *Ceram. Int.*, 2019, **45**(9), 11325–11334.

22 S. Obregón, G. Amor and A. Vázquez, Electrophoretic deposition of photocatalytic materials, *Adv. Colloid Interface Sci.*, 2019, **269**, 236–255.

23 I. Jellal, K. Nouneh, H. Toura, *et al.*, Enhanced photocatalytic activity of supported Cu-doped ZnO nanostructures prepared by silar method, *Opt. Mater.*, 2021, **111**, 110669.

24 B. Zhang, L. He, T. Yao, *et al.*, Simultaneous photoelectrocatalytic water oxidation and oxygen reduction for solar electricity production in alkaline solution, *ChemSusChem*, 2019, **12**(5), 1026–1032.

25 H. Masuda and K. Fukuda, Ordered metal nanohole arrays made by a two-step replication of honeycomb structures of anodic alumina, *Science*, 1995, **268**(5216), 1466–1468.

26 X. Chen and S. S. Mao, Titanium dioxide nanomaterials: synthesis, properties, modifications, and applications, *Chem. Rev.*, 2007, **107**(7), 2891–2959.

27 D. Gong, C. A. Grimes, O. K. Varghese, *et al.*, Titanium oxide nanotube arrays prepared by anodic oxidation, *J. Mater. Res.*, 2001, **16**(12), 3331–3334.

28 Y. Wei, B. Han, Z. Dong, *et al.*, Phosphomolybdic acid-modified highly organized TiO_2 nanotube arrays with rapid photochromic performance, *J. Mater. Sci. Technol.*, 2019, **35**(9), 1951–1958.

29 L. He, Q. Liu, S. Zhang, *et al.*, High sensitivity of TiO_2 nanorod array electrode for photoelectrochemical glucose sensor and its photo fuel cell application, *Electrochem. Commun.*, 2018, **94**, 18–22.

30 Y. Zhao, L. Zhu, Y. Yu, *et al.*, Facile one-pot preparation of Ti^{3+}, N co-doping TiO_2 nanotube arrays and enhanced photodegradation activities by tuning tube lengths and diameters, *Catal. Today*, 2019, 563–572.

31 J. M. Macak, H. Tsuchiya, A. Ghicov, *et al.*, TiO_2 nanotubes: self-organized electrochemical formation, properties and applications, *Curr. Opin. Solid State Mater. Sci.*, 2007, **11**(1–2), 3–18.

32 S. Das, R. Zazpe, J. Prikryl, *et al.*, Influence of annealing temperatures on the properties of low aspect-ratio TiO_2 nanotube layers, *Electrochim. Acta*, 2016, **213**, 452–459.

33 C. Ai, P. Xie, X. Zhang, *et al.*, Explaining the enhanced photoelectrochemical behavior of highly ordered TiO_2 nanotube arrays: anatase/rutile phase junction, *ACS Sustainable Chem. Eng.*, 2019, **7**(5), 5274–5282.

34 H. Fan, S. Zhang and X. Zhu, Nitrided TiO_2 nanoparticles/nanotube arrays for better electrochemical properties, *Chem. Phys. Lett.*, 2019, **730**, 340–344.

35 Z. Liu, J. Tian, C. Yu, *et al.*, Solvothermal fabrication of Bi_2MoO_6 nanocrystals with tunable oxygen vacancies and excellent photocatalytic oxidation performance in quinoline production and antibiotics degradation, *Chin. J. Catal.*, 2022, **43**(2), 472–484.

36 W. Fang and W. Shangguan, A review on bismuth-based composite oxides for photocatalytic hydrogen generation, *Int. J. Hydrogen Energy*, 2019, **44**(2), 895–912.

37 F. Zhou, X. Ren and S. Du, Direct evaluation of unsymmetrical dimethylhydrazine with wide concentration range in wastewater by ion chromatography, *Chromatographia*, 2020, **83**(1), 107–113.

38 Q. Hao, C. Xie, Y. Huang, *et al.*, Accelerated separation of photogenerated charge carriers and enhanced photocatalytic performance of g-C_3N_4 by Bi_2S_3 nanoparticles, *Chin. J. Catal.*, 2020, **41**(2), 249–258.

39 X. Lin, M. Sun, Y. Yao, *et al.*, *In situ* construction of N/Ti^{3+} co-doped tri-phasic TiO_2 layer on TiO_2 nanotube arrays to improve photoelectrochemical performance, *Electrochim. Acta*, 2018, **291**, 319–327.

40 D. Huang, X. Liu, X. Wang, *et al.*, The competitive formation mechanism of *n*-nitrosodimethylamine and formaldehyde dimethylhydrazone from 1,1-dimethylhydrazine during ozonation in air: a combined theoretical and experimental study, *Chem. Phys.*, 2019, **522**, 220–227.

41 Y. Huang, Y. Wei, J. Wang, *et al.*, Controllable fabrication of Bi_2O_3/TiO_2 heterojunction with excellent visible-light responsive photocatalytic performance, *Appl. Surf. Sci.*, 2017, **423**, 119–130.

42 D. Xu, Y. Hai, X. Zhang, *et al.*, Bi_2O_3 cocatalyst improving photocatalytic hydrogen evolution performance of TiO_2, *Appl. Surf. Sci.*, 2017, **400**, 530–536.